J. Fluid Mech. (2007), *vol.* 573, *pp.* 191–209.
doi:10.1017/S0022112006003715 Printed in the United Kingdom

Roughness-induced flow instability: a lattice Boltzmann study

FATHOLLAH VARNIK, DOROTHÉE DORNER AND DIERK RAABE

Max-Planck Institut für Eisenforschung, Max-Planck Straße 1, 40237 Düsseldorf, Germany

(Received 12 October 2005 and in revised form 21 July 2006)

Effects of wall roughness/topography on flows in strongly confined (micro-)channels are studied by means of lattice Boltzmann simulations. Whereas wall roughness in macroscopic channels is considered to be relevant only for high-Reynolds-number turbulent flows (where the flow is turbulent even for smooth walls), it is shown in this paper that, in micro-channels, surface roughness may even modify qualitative features of the flow. In particular, a transition from laminar to unsteady flow is observed. It is found that this roughness-induced transition is strongly enhanced as the channel width is decreased. The reliability of our results is checked by computing the viscous shear stress and the Reynolds stress across the channel, their sum following the theoretical prediction for the stress balance perfectly. Furthermore, the solutions obtained obey the transformation rules of the Navier–Stokes equation: When expressed in reduced (dimensionless) units, results for various channel dimensions, forcing term or dynamic viscosity are identical provided that the channel shape and the Reynolds number are unchanged. The time evolution of the velocity fluctuations at the initial stages of the transition to flow instability is monitored. It is found that fluctuations first occur in the vicinity of the rough wall, supporting the interpretation of wall roughness as a source of fluctuations and thus flow instability. In addition to their physical significance, our results provide further evidence for the reliability of the lattice Boltzmann method in dealing with complex unsteady flows.

1. Introduction

Flow instabilities are of considerable importance both from a theoretical point of view and for engineering applications. An important question concerns the effect of the instability on the transport of heat and mass. It is well known that, as the instability develops a turbulent character, both mass and heat are transported throughout the system in a much more efficient way than by mere diffusion, a phenomenon known as turbulent mixing (Pope 2000). Furthermore, drag and lift forces vary considerably as the nature of the flow changes from laminar into a rather chaotic motion.

It has long been recognized that, at least for distances not too far from the wall, surface roughness plays a significant role in determining the flow characteristics. Surface roughness can enhance flow instability through a variety of mechanisms depending on the mean flow characteristics and the size and spatial distribution of the roughness elements.

Owing to its importance for the natural gas pipeline industry, the impact of surface roughness on the mean flow properties and, in particular, on the friction factor has received considerable attention from as early as the beginning of the past century.

In his seminal work during 1930s, Nikuradse measured the skin friction coefficient, C_f, as a function of Reynolds number (Re) for smooth pipes and for pipes with a varying amount of wall roughness. For this purpose, Nikuradse glued sand to the wall as densely as possible with grain sizes s varying from $s = R/15$ to $s = R/507$ (R is the pipe's radius: see Schlichting (1979) for a description of these experiments). As a result of these studies, it was shown that the turbulent character of the flow is enhanced with increasing grain size (Pope 2000).

As first postulated by Prandtl (1925), at high Reynolds number, there is a region close to the wall (inner layer) where the velocity profile is determined by the viscous scales only. Far enough from the wall, on the other hand, viscosity effects on the mean velocity profile are assumed to be negligible (outer layer) (Pope 2000; Mathieu & Scott 2000). This point of view has been extended to take into account the effects of the wall roughness (for a review see, e.g., Raupach, Antonia & Rajagopalan (1991) and references therein). A result of these studies is that wall roughness effects on the mean flow characteristics are restricted to a region in the vicinity of the wall, i.e. for distances, y, smaller than a few times the roughness height, h. In this region, it is assumed that the mean velocity profile can be fully characterized by introducing a length scale, z_0, related to the wall roughness (Raupach *et al.* 1991). In particular,

$$u^+ = \frac{1}{\kappa}\ln(y/z_0) + C + w(y/D). \tag{1.1}$$

In (1.1), $u^+ = U/u_\tau$ ($u_\tau = \sqrt{\tau_w/\rho}$ is the viscous wall velocity, τ_w the shear stress at the wall and ρ the fluid density) is the rescaled velocity, $\kappa = 0.41$ is the von Kármán constant, C is a constant reflecting the boundary condition at the wall and D is half the channel width. The function w is the so-called wake function assumed to be independent of the wall roughness. As seen from (1.1), wall roughness affects the mean velocity profile only via a rescaling of the distance from the wall by a characteristic roughness length.

On the other hand, at large distances from the wall, properties of the mean flow are considered to be essentially independent of the details of the wall roughness (Rotta 1962). In this (outer) region, one expects

$$u^+ = \frac{1}{\kappa}\ln(y^+) + B - \Delta U(z_0) + w(y/D), \tag{1.2}$$

where $B \approx 5.2$ as in the case of smooth surfaces and $y^+ = y/\delta_\nu$ with δ_ν being the viscous wall length defined by $\delta_\nu u_\tau/\nu = 1$ (ν is the kinematic viscosity). Obviously, roughness effects enter (1.2) via the simple (downward) shift of the mean velocity by an amount $\Delta U(z_0)$ only, having no further impact on the y-dependence of the mean velocity.

At high enough Reynolds number, there is an overlap region between the inner and the outer layer, where both (1.1) and (1.2) must hold. This gives a simple expression for the roughness function, $\Delta U(z_0) = (1/\kappa)\ln(z_0^+) + B - C$, where $z_0^+ = z_0/\delta_\nu$ is the rescaled roughness length. It must be emphasized here that the length scale z_0 is not necessarily equal to the (average) roughness height h. Rather it characterizes the whole effect of the wall roughness on the mean flow and thus in general depends on the details of the wall roughness such as shape and distribution of the roughness elements.

So far the effects of the wall roughness on the mean flow properties have been discussed. As recent studies reveal (Krogstad & Antonia 1999), the situation is quite different from what is outlined above if *turbulent quantities* are considered. While the

effects of the surface roughness on the mean flow are indeed limited to a narrow region of a few times the roughness height, turbulent quantities such as various components of the Reynolds stress tensor (for a definition, see below) may exhibit significant dependence on the specific wall roughness over the entire flow region (Krogstad & Antonia 1999).

Krogstad & Antonia (1999), for example, studied surface roughness effects in turbulent boundary layers by comparing measurements over two rough walls with different surface geometries but the same roughness functions with measurements over a smooth wall boundary layer. It was found that various turbulent quantities, such as Reynolds stresses, the rate of turbulent energy production and turbulent diffusion, differ significantly for the two types of roughness studied. They therefore concluded that a roughness function alone is not sufficient in order to model surface roughness effects on turbulent flows accurately.

Note that the above-mentioned experiments were performed at sufficiently high Reynolds numbers so that the flow is turbulent not only for the case of rough walls but also over the smooth wall. It is tempting to ask whether one can switch from a laminar to a turbulent (or at least non-steady) flow by a variation of the surface roughness alone. Recall that, as already indicated by Landau & Lifschitz (1991), the occurrence of flow instability is the result of two major factors: (i) the sensitivity of the system to a perturbation and (ii) the amplitude of the perturbation. Whereas Reynolds number controls the first factor (the higher Re the more sensitive the system is to a given perturbation) a change of the surface roughness may affect the magnitude of the perturbations.

In this report, we address this aspect of the problem via lattice Boltzmann (LB) computer simulations. It will be shown that it is indeed possible to generate flow instabilities by a variation of the surface roughness at a Reynolds number for which the flow over a flat surface is laminar. This is an important observation providing new insight into the nature of flow instabilities.

In a turbulent boundary layer, the viscous length, δ_ν, decreases with increasing Reynolds number, an empirical estimate is given by $D/\delta_\nu = 0.09\,Re^{0.88}$ (Pope 2000), where D is half the channel width and $Re = UD/\nu$ is the Reynolds number. As a result, δ_ν may be quite small at high Reynolds numbers. Taking the example given in Pope (2000), at $Re = 10^5$ and for a channel with a half-width $D = 2\,\mathrm{cm}$, the viscous length is estimated to be $\delta_\nu \approx 10^{-5}\,\mathrm{m}$. A location as 'far' as $y^+ = 100$ is, therefore, at a distance of $\approx 1\,\mathrm{mm}$ from the wall. Conducting measurements in the viscous wall region of laboratory flows thus becomes progressively more difficult at high Reynolds number.

In a lattice Boltzmann simulation, on the other hand, it is straightforward to make the smallest relevant length scale equal to the lattice spacing. The price to pay is that large length scales are hardly accessible within an LB simulation if no use is made of some sort of turbulent modelling (Filippova *et al.* 2001; Chen *et al.* 2003). A drawback of turbulent modelling is, however, the use of closure relations which, if well adapted to the problem of interest, may give satisfactory results but need not be valid in general. We will exclusively apply the 'bare' lattice Boltzmann without any use of turbulent constitutive relations. In this form, the LB method provides an alternative 'first principle' approach to the study of flow instabilities and thus can be considered as complementary to real experiments where much larger scales are accessible.

Despite the above-mentioned limitations, an important advantage of the lattice Boltzmann method (as well as other, more conventional, Navier–Stokes solvers) is that, within a simulation, one has access to the complete information on the flow

field. This allows, at least in principle, a computation of any quantity of interest in the course of simulation as far as it can be expressed in terms of fluid velocity and density. Examples of such quantities for an unstable flow are the Reynolds stress tensor, energy dissipation rate and two-point correlation functions of the velocity fluctuations, to name just a few.

In order to concentrate on the principal question addressed above, we restrict our attention to the case of two-dimensional flows. We are aware of the fact that two-dimensional turbulence may be qualitatively different from its three-dimensional-counterpart. This is best seen by taking the curl of the Navier–Stokes (NS) equation and thus obtaining the evolution equation of the vorticity, $\boldsymbol{\omega} = \nabla \times \boldsymbol{U}$. For an incompressible fluid in three dimension, this leads to

$$\frac{\partial \boldsymbol{\omega}}{\partial t} + \boldsymbol{U} \cdot \nabla \boldsymbol{\omega} = \nu \nabla^2 \boldsymbol{\omega} + \boldsymbol{\omega} \cdot \nabla \boldsymbol{U}. \tag{1.3}$$

Repeating the same procedure in two dimensions, one can easily show that no vortex stretching term ($\boldsymbol{\omega} \cdot \nabla \boldsymbol{U}$) exists in two-dimensions (Pope 2000). The vorticity is hence conserved in two-dimensional inviscid flow ($\nu = 0$). Close to the walls, however, the first term on the right-hand side of (1.3) becomes dominant even at low viscosities thus giving rise to a complex scenario for the time evolution of the vorticity.

After a short introduction to the lattice Boltzmann approach, we validate the method using simple shear flows for which analytic/numeric solutions are easily obtained. Results on roughness-induced flow instability are discussed in § 4.

2. Lattice Boltzmann method

In the past decade, kinetic theory and most notably the lattice Boltzmann method (McNamara & Zanetti 1988; Higuera, Succi & Benzi 1989; Benzi, Succi & Vergassola 1992; Qian, d'Humieres & Lallemand 1992; Chen *et al.* 2003) has received increasing attention as an efficient tool for the study of a variety of fluid flow problems such as two-phase flow through porous media (Gunstensen & Rothman 1993), particle–fluid suspensions (Ladd & Verberg 2001; Ahlrichs & Dünweg 1999) and high-Reynolds-number turbulent flows (Succi *et al.* 2002).

There are excellent monographs Succi (2001), Rothman & Zaleski (1997), Wolf-Gladrow (2000) and comprehensive review articles Chen & Doolen (1998), Ladd & Verberg (2001), Raabe (2004) on the LB method and the historically related lattice gas cellular automata (LGCA) (Frisch, Hasslacher & Pomeau 1986; Frisch *et al.* 1987). Here, we give a short introduction to the method.

A simplified view of the lattice Boltzmann method may be presented as follows: A fluid portion residing at a given point, $\boldsymbol{x}$, in space is divided into a small number of parcels, f_i, each moving with a well-defined velocity, $\boldsymbol{c}_i$, on a lattice (figure 1). During the time step $t \to t + 1$ (note that $\Delta t = 1$), the fluid parcel, $f_i(\boldsymbol{x}, t)$, is first relaxed to its local equilibrium, $f_i^{\mathrm{eq}}(\boldsymbol{x}, t)$, at a rate of ω,

$$f_i'(\boldsymbol{x}, t) = f_i(\boldsymbol{x}, t) - \omega(f_i(\boldsymbol{x}, t) - f_i^{\mathrm{eq}}(\boldsymbol{x}, t)), \tag{2.1}$$

and then freely propagated to the site $\boldsymbol{x} + \boldsymbol{c}_i$,

$$f_i(\boldsymbol{x} + \boldsymbol{c}_i, t + 1) = f_i'(\boldsymbol{x}, t). \tag{2.2}$$

Here, the post-collision population, f_i', is introduced to underline the formal separation of the relaxation and propagation steps. The relaxation rate is closely related to the fluid dynamic viscosity, ν. For the D2Q9-model used in the present

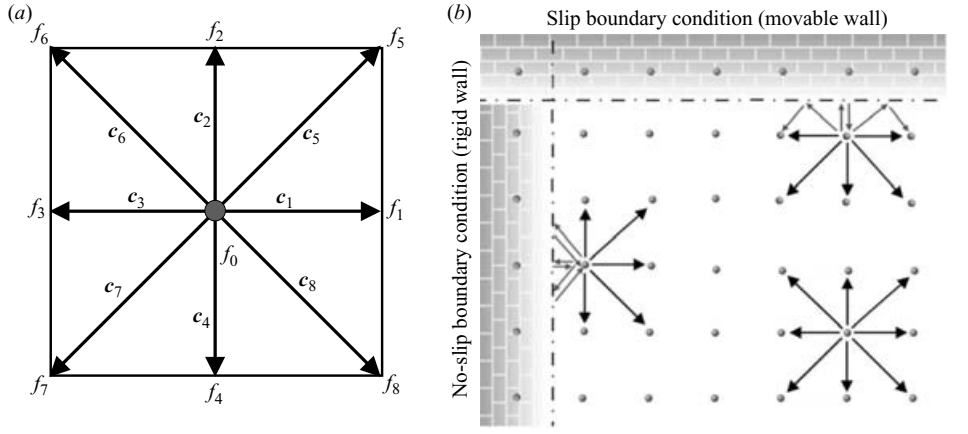

FIGURE 1. Schematic view of the two-dimensional nine-velocity (D2Q9) lattice Boltzmann model (*a*) and of two common types of boundary conditions (*b*).

work (see below), the relation between ω and ν is

$$\nu = \frac{1}{6}\left(\frac{2}{\omega} - 1\right). \tag{2.3}$$

The local equilibrium distribution, f_i^{eq}, is usually taken as a second-order expansion of the Maxwell velocity distribution leading to

$$f_i^{\mathrm{eq}} = \rho w_i \left[1 + \frac{1}{c_s^2}\boldsymbol{u}\cdot\boldsymbol{c}_i + \frac{1}{2c_s^4}\left[(\boldsymbol{u}\cdot\boldsymbol{c}_i)^2 - c_s^2\boldsymbol{u}\cdot\boldsymbol{u}\right]\right], \tag{2.4}$$

where c_s is the sound speed and w_i is a set of weights normalized to unity. For the two-dimensional nine-velocity model (D2Q9) used in our studies (see figure 1 for an illustration) $w_0 = 4/9$, $w_1 = w_2 = w_3 = w_4 = 1/9$ and $w_5 = w_6 = w_7 = w_8 = 1/36$ (see Wolf-Gladrow (2000) for a short but comprehensive derivation). Once the discrete populations, f_i, are known, fluid density, $\rho(\boldsymbol{x}, t)$, and velocity, $\boldsymbol{u}(\boldsymbol{x}, t)$, at a given point and time are obtained via

$$\rho = \sum_i f_i(\boldsymbol{x}, t) \quad \text{and} \quad \rho\boldsymbol{u} = \sum_i f_i(\boldsymbol{x}, t)\boldsymbol{c}_i. \tag{2.5}$$

Figure 1(*a*) depicts a view of the two-dimensional nine-velocity (D2Q9) lattice Boltzmann model used in our simulations. During the free propagation step, the population f_i is transported along the velocity vector $\boldsymbol{c}_i$ ($i = 0, 1, \ldots, 8$). The zero-velocity population, f_0, ensures correct hydrodynamic behaviour in the compressible regime, i.e. at high Mach numbers (fluid velocity/sound speed). Two common types of boundary conditions are illustrated in figure 1(*b*). For fluid particles moving toward a solid node on the left wall both the perpendicular and the parallel components of the velocity vector are reversed. This is easily achieved by sending the incoming populations back toward the nodes they came from (bounce back rule).

For a planar wall, this leads to the so-called non-slip boundary condition with the zero velocity plane lying approximately halfway between the solid and the neighbouring fluid nodes. In order to obtain a slip boundary condition (moving wall), on the other hand, the incoming populations are reflected like light rays on a mirror, i.e. the vertical component of the velocity is reversed while keeping the

tangential velocities unchanged (top wall). In our simulations, we will use the non-slip boundary condition only (by applying the bounce back rule as described here).

Note that the bounce back rule is second-order accurate only for boundaries which are aligned with the grid line. In the case of non-aligned surfaces, such as we study in the present work, the accuracy is reduced to first order. However, as a study of the grid size dependence reveals (figure 7), this numerical noise is small compared to the (physical) fluctuations of the velocity field originating from the wall roughness.

As can be seen from the above description, the solution for the particle distribution function, f_i, is explicit and local. The corresponding code is, therefore, easy to implement and, locality being a precondition for an efficient parallelization, natural to parallelize. Furthermore, within the lattice Boltzmann method, any point on the lattice can be defined as a solid node, thus providing a simple framework for the simulation of the flow in arbitrarily complex geometries.

In the following, all quantities are expressed in LB units. The unit of length is the internode spacing, $\Delta x \equiv 1$. The time is measured in units of an iteration step, $\Delta t \equiv 1$. This fixes the unit of the velocity $\Delta x/\Delta t \equiv 1$. Comparison with real situations is easily done by first identifying the Reynolds number and then applying appropriate transformations.

3. Validation of the method: Stokes flow

In order to check the reliability of the method and its implementation, we first performed a series of simulations at low Reynolds number of flow between two parallel walls (Poiseuille-type flow). It must be emphasized here that the present test deals with a situation where the nonlinear (advective) term of the NS-equation is identically zero. Therefore, this section does not provide a check of the LB method with respect to the full NS-equation.

A more telling test will be provided in the next section when we discuss the roughness-induced transition toward flow instability. There, we will see that in the unstable regime (where the flow exhibits strong nonlinearities), the solutions obtained via lattice Boltzmann simulations obey the transformation rules of the NS-equation: When expressed in reduced (dimensionless) units, solutions obtained for various channel dimensions, forcing term or dynamic viscosity are identical provided that the channel geometry and the Reynolds number are unchanged (figure 7). This result is not trivial since the LB approach is kinetic in nature and thus quite different from a numerical solution of the NS-equation, where the scaling behaviour is directly build up in the approach. At the same time, the test will also provide evidence for the independence of the results of the grid size.

The present study of a Stokes flow is interesting since it not only provides a check of the simulation code for the case of the linear NS-equation, but also yields useful information on the parameter range where the LB method works well and is free of undesired effects (such as partial slip at high dynamic viscosities, see below). Furthermore, the study of the laminar channel flow will naturally introduce the so-called momentum diffusion time, which sets the time scale for the onset of a steady-state flow. This is an important quantity as it tells us how long a simulation should run in order to avoid transient effects, i.e. in order to make sure that statistical properties of the flow are time-independent.

At time $t = 0$ the fluid is at rest. In order to drive the flow, a constant force density, $\boldsymbol{g} = \rho g \boldsymbol{e}_x$ ($\boldsymbol{e}_x$ is the unit vector in x-direction, ρ is the fluid density and g is an acceleration) is applied to the fluid for $t \geqslant 0$. The situation considered here is thus reminiscent

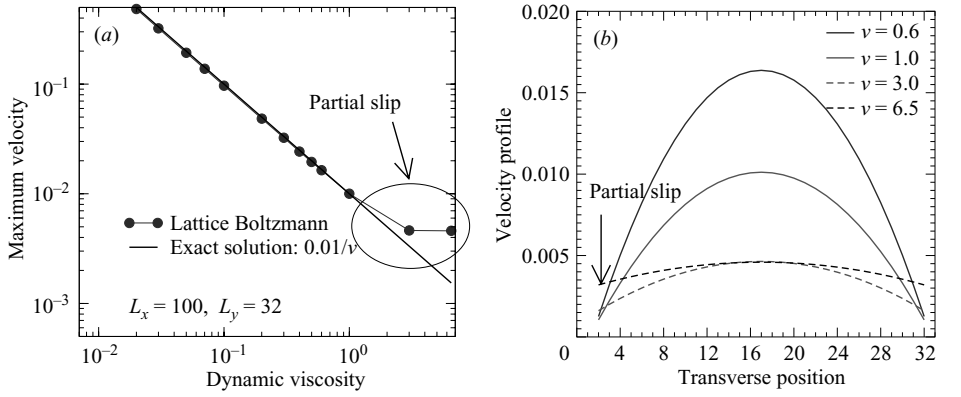

FIGURE 2. (*a*) Log-log plot of the streaming velocity in the middle of the channel, U_0, versus dynamic viscosity. Solid line gives the exact solution, (3.2). (*b*) Velocity profile for some selected dynamic viscosities indicating the presence of a finite slip velocity at the wall at high dynamic viscosities.

of gravity-driven flow. For the two-dimensional planar geometry considered here, the Stokes equation is

$$\frac{\partial U_x}{\partial t} = \nu \frac{\partial^2 U_x}{\partial y^2} + g, \tag{3.1}$$

where we have used that the flow is laminar and one-directional ($U_y = 0$). In the steady state ($\partial U_x/\partial t = 0$) the exact solution of (3.1) is known: $U_x(y) = U_0(1-4y^2/L_y^2)$, where y denotes the transverse coordinate ($y = 0$ corresponding to the midpoint between the plates), L_y is the separation of the plates and

$$U_0 = \frac{L_y^2 g}{8\nu} \tag{3.2}$$

is the maximum flow velocity observed in the middle of the channel. Equation (3.2) provides a simple way to test the lattice Boltzmann simulation. For this purpose, we have performed simulations of a system of size 100×32 for various values of the dynamic viscosity ν. The value of external force was chosen as $g = 8 \times 10^{-5}$.

Figure 2(*a*) provides a first test of our simulations by plotting the maximum velocity in the channel, U_0, versus dynamic viscosity. Simulation results are compared to the exact solution, (3.2). For $\nu \leqslant 1$, the simulated data follow the theoretical line, while at higher viscosities deviations occur. An inspection of the velocity profile for some selected dynamic viscosities (figure 2*b*) shows that, for $\nu > 1$, the velocity at the wall is not zero, indicating the onset of partial slip. At low dynamic viscosities ($\nu \leqslant 1$) on the other hand, the non-slip boundary condition is quite well satisfied.

Thus, at high dynamic viscosities, the bounce back rule is not able to perfectly ensure the non-slip boundary condition and a partial slip at the walls occurs. This finite slip is closely related to the kinetic nature of the LB method (Cornubert, d'Hummiières & Levermore 1991; Ginzbourg & d'Humières 1996, 2003; Luo 1997; He & Luo 1997) and introduces the relevance of Knudsen issues for the problem under consideration.

The Knudsen number (Kn = mean free path/characteristic length) is a measure of the validity of the hydrodynamic limit for the problem of interest (the lower Kn, the better this limit is approached). It is, therefore, instructive to estimate the ratio of the

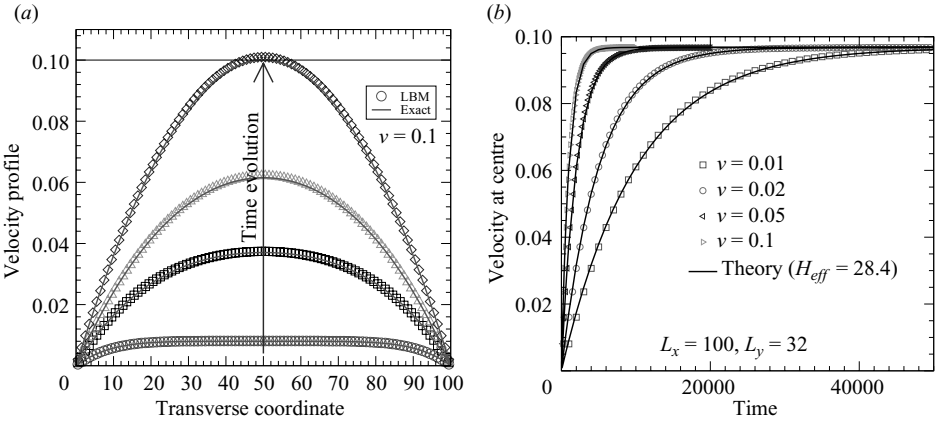

FIGURE 3. (*a*) Time evolution of the velocity profile from $U_x(y, t = 0) = 0$ to the steady state (system size $= 100 \times 100$). Simulated velocity profiles are compared to numerical solution of the Stokes equation, (3.1). (*b*) Maximum velocity versus time for various dynamic viscosities (system size $= 100 \times 32$). The solid lines are fits to (3.3).

mean free path of a fluid particle to the smallest length occurring in the system, i.e. to the lattice pitch. This is done by noting that the mean free path $l = \nu/c_s$, where ν is the dynamic viscosity and c_s the speed of sound in the fluid. In order to proceed further, it is useful to introduce dimensionless lattice Boltzmann quantities ν^{LB} and c_s^{LB} via $\nu = \nu^{LB}\Delta x^2/\Delta t$ and $c_s = c_s^{LB}\Delta x/\Delta t$. This gives $l = \nu^{LB}/c_s^{LB}\Delta x$. Thus, the Knudsen number associated with a lattice pitch is given by $Kn(\Delta x) = l/\Delta x = \nu^{LB}/c_s^{LB}$. Noting that c_s is usually of order unity ($c_s = 1/\sqrt{3} \approx 0.6$ for the two-dimensional nine-velocity model used in this work) it follows that the largest Knudsen number occurring in the problem is of order the dimensionless dynamic viscosity, ν^{LB} (we assume that the problem does not contain length scales smaller than Δx). As a consequence, $Kn(\Delta x) > 1$ for $\nu^{LB} > 1$. In other words, the basic requirement of low Knudsen number is violated at LB dynamic viscosities of order unity or higher.

In the present case, however, we are interested in the opposite limit of low viscosity (high Reynolds number). Indeed, for a study of the roughness-induced flow instability (§ 4) $\nu^{LB} = 0.001$ is used, which means that the largest Knudsen number occurring in our simulation studies of roughness effects is $Kn(\Delta x) \approx 1.67 \times 10^{-3}$. The hydrodynamic limit is thus very well satisfied even on the scale of internode spacing and thus for all values of the roughness asperties used in our simulations. In the following, we drop the superscript 'LB'.

Next we consider the time evolution of the flow from $t = 0$ until the steady state is reached. Figure 3(*a*) illustrates the velocity profiles measured for various time steps, t, after the external force is switched on. Again, the lattice Boltzmann simulation results are compared to numerical solution of the Stokes equation (3.1) and excellent agreement is found. As seen from this plot, at early stages of the flow only the fluid particles in the proximity of the wall are decelerated, whereas the remaining part of the system accelerates with a constant rate as if no walls were present. This gives rise to the observed plateau in the velocity profile in the inner part of the system. The width of the plateau decreases with time as progressively larger parts of the fluid 'feel' the presence of the boundaries, and eventually a parabolic velocity profile forms. In order to obtain an approximate analytical expression for the variation with time of the mid-channel velocity, $U_0(t)$, we insert the ansatz $U_x(y, t) = U_0(t)(1 - (2y/L_y)^2)$

in the Stokes equation (3.1). One then obtains an equation for $U_0(t)$), which can be solved with the result

$$U_0(t) = gt_d(1 - \exp(-t/t_d)), \tag{3.3}$$

where $t_d = L_y^2/(8\nu)$ is the characteristic time scale for the establishment of the steady state. Figure 3(*b*) depicts simulated results on $U_0(t)$ for various choices of the dynamic viscosity. Fits to (3.3) are also shown. As seen from this figure, (3.3) yields a satisfactory description of the time dependence of $U_0(t)$ if, instead of $L_y = 32$, a slightly smaller effective width of $H_{\text{eff}} = 28.4$ is used. This deviation is, however, not unexpected as we ignored the variation of the shape of the velocity profile with time. Taking this fact into account, the observed agreement between the approximate theory and simulation is strikingly good. An important consequence of this agreement is the relevance of the time scale, t_d, for the establishment of a steady state.

Note that the dependence of t_d on the dynamic viscosity, ν, and on the length, L_y, can also be obtained without explicit solution of the Stokes equation. For this purpose, one resorts to scaling arguments. On physical grounds, t_d is expected to depend on ν and on a characteristic length, say L_y, only. Now, apart from dimensionless pre-factors, L_y^2/ν is the unique combination of ν and L_y with the dimension of time. This type of reasoning, however, is not able to yield the correct pre-factor, which, in the present case, makes almost one order of magnitude of difference.

Noting that the time necessary to simulate one LB iteration scales with the system size and thus with L_y^2 (in two dimensions), and taking into account the fact that at least t_d iterations are required before time-independent quantities can be computed, it follows that the total computation time scales as L_y^4. As a consequence, a study of large systems becomes prohibitively expensive in terms of computation time. This has motivated further developments of the lattice Boltzmann method such as grid-refinement (Filippova & Hänel 1998; Dupuis & Chopard 2003) and finite volume (Xi, Peng & Chou 1999) approaches allowing areduction of this scaling at least to some extent. These approaches, however, increase the complexity of the code considerably by requiring a careful decomposition of the computational domain (which, in the case of our studies, may strongly depend on the shape and distribution of roughness elements), a proper choice of the grid size in each sub-domain and including the continuity aspects at the sub-domain boundaries.

We do, however, aim at keeping the simulation methodology as simple as possible in order to focus on the physical phenomenon of interest. Therefore, we will use the 'plain' LB approach without any extensions. Fortunately, as will be shown below, interesting phenomena can be observed for system sizes within the range of one day to one week simulation time on a single Itanium 1.3 GHz CPU.

4. Results on roughness-induced instability

Effects of the surface roughness on flow instability are considered in this section. For this purpose, we study the flow through a channel composed of a flat wall and a wall with an idealized type of roughness, of zig-zag type. A schematic view of the simulation box is shown in figure 4(*a*). A zig-zag surface may easily be characterized by its wavelength, λ, and its height h. Therefore, we refer to a given zig-zag surface by indicating its height and the half-wavelength in the form $h : \lambda/2$ ($h/(\lambda/2)$ being the magnitude of the surface slope). Flow velocity versus time is recorded at nine points placed equidistantly along the line $x = 40$ (the array of circles in figure 4*a*). It must be emphasized here that the phenomenon we discuss is not restricted to this

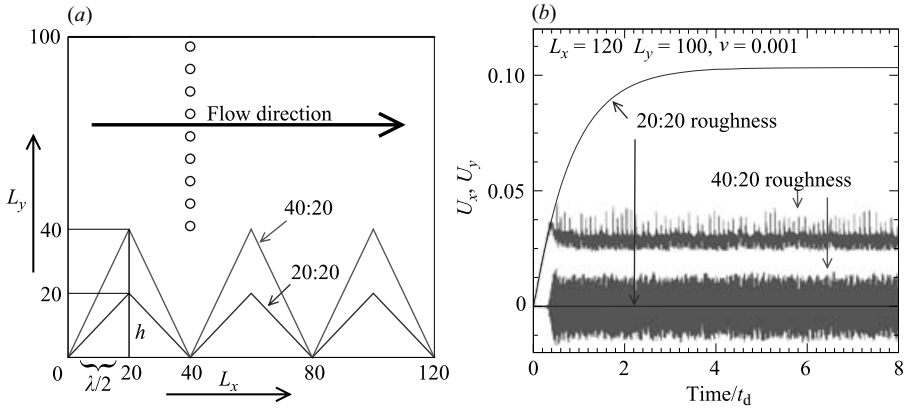

FIGURE 4. (*a*) A sketch of the simulation box. In the notation $a : b$, the first argument indicates the height of the roughness tip and the second the half-width of the baseline (a/b = slope). Flow velocity versus time is recorded at nine points placed equidistantly along the line $x = 40$ (array of circles). Note that the region below the zig-zag line is filled with solid particles (not shown for clarity). (*b*) Time evolution of U_x and U_y, measured at a point in the middle of the flow region.

specific choice of the surface roughness but also occurs for other choices of (periodic) distribution of triangular obstacles as well as for a random distribution of obstacle elements.

Figure 4(*b*) illustrates how a variation of the surface roughness alone may give rise to flow instability. For this purpose, the fluid velocity in the middle of the flow region (midway between the roughness tip and the top wall) is shown versus time for the flow over a 20:20 and 40:20 ('rougher') zig-zag surface. In both cases, the simulation is started with a quiescent fluid ($\boldsymbol{U}(t = 0) = \boldsymbol{0}$) and an external body force of $g = 8\nu U_0/(L_y - h)^2$ is switched on at $t = 0$ (equation (3.2)). This choice ensures that, in the steady state, the maximum velocity in the channel reaches a value close to U_0, provided that the flow is laminar (the subtraction of the roughness height, h, from L_y takes into account the reduction of the effective channel width due to the wall roughness).

In the case of the channel with a 20:20 zig-zag surface, the fluid velocity in the direction parallel to the wall, U_x, increases continuously and smoothly until it reaches the steady state after a time of order $t_d = (L_y - h)^2/(8\nu)$ as estimated from a study of the Stokes flow in a planar channel of effective width $L_y - h$. The vertical component of the fluid velocity, U_y, on the other hand, remains zero at all times.

A qualitative change in the flow behaviour is, however, observed in figure 4(*b*) as the roughness height is increased from 20 to 40. Now, both U_x and U_y exhibit strong fluctuations indicative of instability. The flow instability also manifests itself in a drop (by more than a factor of two) of the mean mid-channel velocity, signalling a higher friction force and thus a higher energy dissipation rate.

It must be emphasized here that, in addition to the difference in dimensionality between our simulations (two-dimensional) and real experiments (three-dimensional), length scales resolved within our simulations cover two orders of magnitude only. Noting that full features of rough wall turbulence develop over many decades in length (Pope 2000), it is not possible to observe all features of fully developed turbulence within the present simulation studies. The situation we study instead corresponds to the transition regime, where some but not all features of turbulence appear.

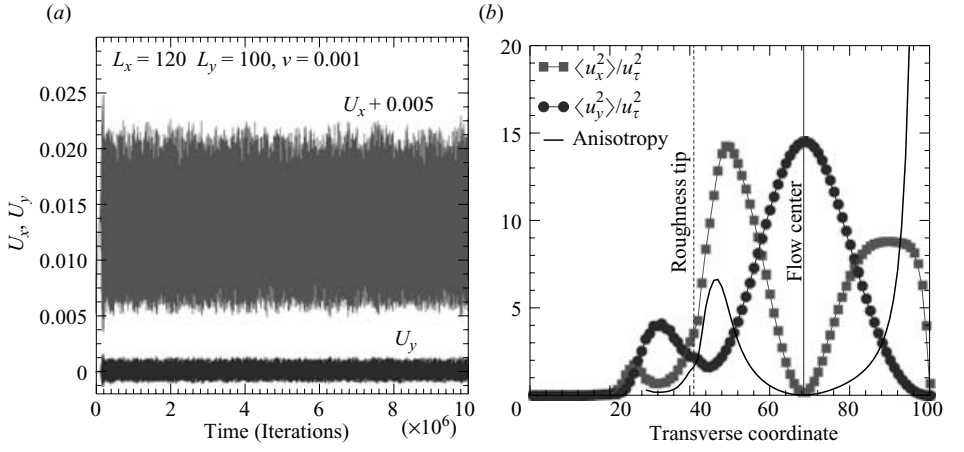

FIGURE 5. (*a*) U_x and U_y versus time for a point in the close vicinity of the smooth wall in the channel with a 40:20 zig-zag wall. (*b*) Standard deviation of the velocity fluctuations divided by the square of the wall friction velocity, u_τ. The anisotropy curve gives the variation of $\langle u_x^2\rangle/\langle u_y^2\rangle$ across the channel.

An interesting observation which is also known from textbooks on turbulence, is shown in figure 5. Figure 5(*a*) shows U_x and U_y at $x = 40$, $y = 97$, i.e. at a point quite close to the smooth wall. Obviously, close to the wall, much stronger velocity fluctuations occur in the flow direction than in the perpendicular one. This observation can be made quantitative by determining the standard deviations of the velocity field, $\langle u_x^2\rangle$ and $\langle u_y^2\rangle$ ($\boldsymbol{u} = \boldsymbol{U} - \langle \boldsymbol{U}\rangle$) across the channel. For this purpose, we plot in figure 5(*b*) the spatial variation of $\langle u_x^2\rangle/u_\tau^2$ and $\langle u_y^2\rangle/u_\tau^2$ and their ratio, known as the anisotropy parameter ($u_\tau = \sqrt{\tau_w/\rho}$ is the so-called wall friction velocity, τ_w being the viscous shear stress at the wall; see the discussion of (4.2)).

Let us focus our attention on the vicinity of the top wall (transverse coordinate larger than 70) in figure 5(*b*). In accordance with observations from turbulent channel flow (see e.g. Mathieu & Scott 2000, p. 108ff)), $\langle u_x^2\rangle$ exhibits a maximum whereas $\langle u_y^2\rangle$ increases continuously with larger distances from the wall. The velocity fluctuations thus exhibit an enhanced anisotropic behaviour. While $\langle u_x^2\rangle$ is larger close to the wall, it becomes far smaller than $\langle u_y^2\rangle$ at greater distances from the wall. This anisotropy is best seen in the behaviour of $\langle u_x^2\rangle/\langle u_y^2\rangle$, which exhibits the largest values close to the wall, in accordance with experimental observations.

Note that the magnitude of the velocity fluctuations is larger close to the rough wall compared to the vicinity of the smooth wall, whereas the *anisotropy* behaves in the opposite way. A possible explanation of the weaker anisotropy in the proximity of the zig-zag surface is as follows. The anisotropy reflects the fact that, close to the wall, velocity fluctuations parallel to the wall are enhanced compared to those in the perpendicular direction. A proper measure of anisotropy must, therefore, take into account the actual orientation of the wall. In other words, close to a zig-zag surface, u_x^2/u_y^2 is no longer an appropriate measure of anisotropy since both u_x and u_y contain components parallel and perpendicular to the surface.

Next we examine the equation governing the behaviour of the mean velocity profile. In contrast to a laminar flow, where the velocity profile is directly related to the applied pressure gradient via $\partial p/\partial x = \nu\rho\partial^2 U_x/\partial y^2$, one finds for an unsteady flow

(Pope 2000; Mathieu & Scott 2000),

$$\frac{\partial\langle p\rangle}{\partial x} = \frac{\partial}{\partial y}\left[\nu\rho\frac{\partial\langle U_x\rangle}{\partial y} - \rho\langle u_x u_y\rangle\right], \tag{4.1}$$

where $\langle p\rangle$ is the average pressure. The second term on the right-hand side of (4.1), $-\rho\langle u_x u_y\rangle$, is the so-called Reynolds stress and plays a crucial role in unsteady flows. In our simulations, we apply a constant pressure gradient via the body force ρg (equation (3.1)). Inserting this information into (4.1) and integrating over y yields

$$\nu\rho\frac{\partial\langle U_x\rangle}{\partial y} - \rho\langle u_x u_y\rangle = \tau_w + \rho g(y - y_w), \tag{4.2}$$

where y_w is the position of the wall. The physical meaning of τ_w is clarified by noting that the velocity field is identically zero at the wall and so are its fluctuations. Hence, $\langle u_x u_y\rangle = 0$ for $y = y_w$. It follows then from (4.2) that $\tau_w = \nu\rho\partial\langle U_x\rangle/\partial y|_{y=y_w}$. In other words, τ_w is the shear stress at the wall.

In a laminar flow, the contribution of the Reynolds stress term in (4.2) is negligibly small compared to that of the velocity gradient term, whereas it becomes dominant in the case of turbulent flows (Pope 2000; Mathieu & Scott 2000). The relative magnitude of the Reynolds stress with respect to the viscous stress is, therefore, an important measure of the unsteady/chaotic character of the flow.

In order to examine this aspect, both the Reynolds stress and the viscous shear stress are measured during our simulations. Note that, in addition to an estimate of the shear stress, τ_s, via the partial derivative of the mean velocity profile, the lattice Boltzmann approach provides an alternative way of computing the viscous shear stress (Mei *et al.* 2002):

$$\tau_s = \left(1 - \frac{\omega}{2}\right)\sum_i \left(f_i - f_i^{eq}\right)c_{ix}c_{iy}. \tag{4.3}$$

An advantage of this approach compared to the partial derivative is that it is local and thus provides an accurate measure of the shear stress also at fluid nodes in the immediate vicinity of the wall. The Reynolds stress is computed by time averaging. In order to avoid effects of transients, the collection of fluctuating quantities is started after a time of $5t_d$ only. As can be seen from figure 4, this delay time is large enough to ensure the absence of any transients.

Results on the viscous shear stress and the Reynolds stress are shown in figure 6 for the two above-mentioned choices of zig-zag walls. Figure 6(*a*) depicts profiles of the viscous shear stress, $\nu\rho\partial\langle U_x\rangle/\partial y$, the Reynolds stress, $-\rho\langle u_x u_y\rangle$, and their sum for a flow in a channel made up of a smooth wall (placed at $y = 101$) and a 20:20 zig-zag surface. The Reynolds number is estimated by using the maximum velocity in the channel, $U_0 = 0.12$, the effective channel half-width $(L_y - h)/2 = 40$ and the dynamic viscosity $\nu = 0.001$. This gives $Re = 4800$. With the exception of a region below the roughness height, the Reynolds stress is practically negligible overall in the system and the viscous shear stress obeys (4.2) with $\tau_w = 5.1\times10^{-7}$, $\rho g = 1.3\times10^{-8}$ and $y_w = 21$.

Data shown in figure 6(*b*) (a 40:20 zig-zag surface), on the other hand, exhibit a remarkable contrast to figure 6(*a*). Now, it is the Reynolds stress which dominates the response of the fluid to the imposed body force. Nevertheless, it is worth noting that, in the close vicinity of the smooth wall (to the right of the plot) the viscous stress becomes dominant, a behaviour reminiscent of the viscous sublayer in turbulent flows (Pope 2000; Mathieu & Scott 2000). Note also that the sum of viscous and Reynolds

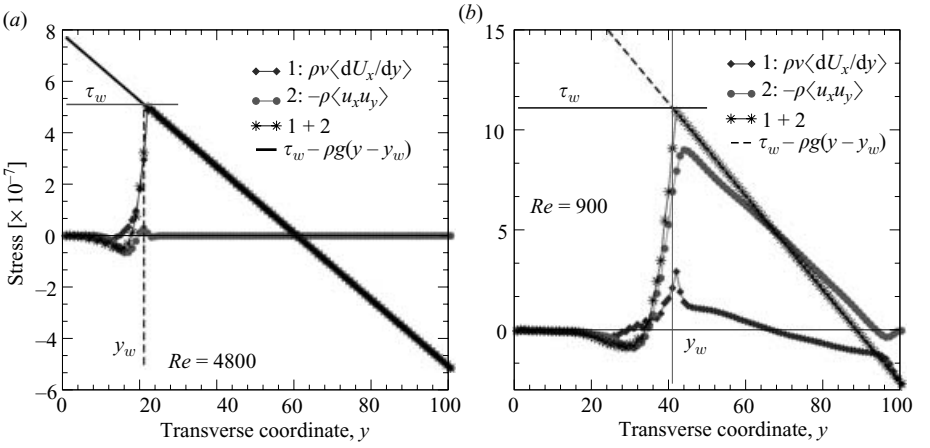

FIGURE 6. (*a*) Profiles of the viscous shear stress, $\nu\rho\partial\langle U_x\rangle/\partial y$, the Reynolds stress, $-\rho\langle u_x u_y\rangle$, and their sum for a flow in a channel made up of a smooth wall and a 20:20 zig-zag surface. The solid line is a fit to (4.2). (*b*) As in (*a*), but for a 40:20 zig-zag surface.

stresses is well described by (4.2) which is an exact relation derived from the NS-equation. This confirms the reliability of the lattice Boltzmann method in capturing unsteady flow behaviour. Similar to figure 6(*a*), we estimate the Reynolds number by noting that $U_0 \approx 0.03$, $(L_y - h)/2 = 30$ and $\nu = 0.001$. This yields $Re \approx 900$. This value lies more than a factor of 5 below that of figure 6(*a*). Thus, a higher roughness height leads to significant instability despite a much lower Reynolds number.

In addition to the above-discussed analysis of the stress balance in the light of (4.2), the data shown in figure 7 provide a further, non-trivial, test of the reliability of the simulation results. Here, the question investigated is whether the solutions obtained within lattice Boltzmann simulations obey the transformation rules as expected from the structure of the NS-equations: for a given Reynolds number and channel geometry/shape (and under exactly the same boundary and initial conditions) the solution of the Navier–Stokes equation is unique, provided that it is expressed in appropriate dimensionless units.

The test shown in figure 7 is twofold. The upper panels examine a transformation where only the time and the velocity scales are changed (in a way that the Reynolds number remains constant), whereas in the lower panels the spatial dimensions of the channel also are varied.

For the first of these, figure 7(*a*) depicts U_x and U_y versus time for two choices of the characteristic velocity, U_0. Note that, in order to keep the Reynolds number constant, the dynamic viscosity is varied by the same factor as the characteristic velocity. This leads to a corresponding variation of the relevant time scale, t_d. Figure 7(*b*) depicts exactly the same data as in (*a*), now expressed in units of U_0 and t_d. Despite the highly nonlinear nature of the flow (which is also reflected in the time dependence of U_x and U_y), the uniqueness of the solution in terms of dimensionless quantities is nicely reproduced.

Figure 7(*c*, *d*) checks whether our results satisfy the scaling behaviour of the solutions of the NS-equation with respect to transformations also involving the spatial scales. Here, the Reynolds stress is depicted across the channel for two choices of channel size (120×50 and 240×100) and two values of the characteristic velocity. The Reynolds number as well as the channel shape and initial conditions are the

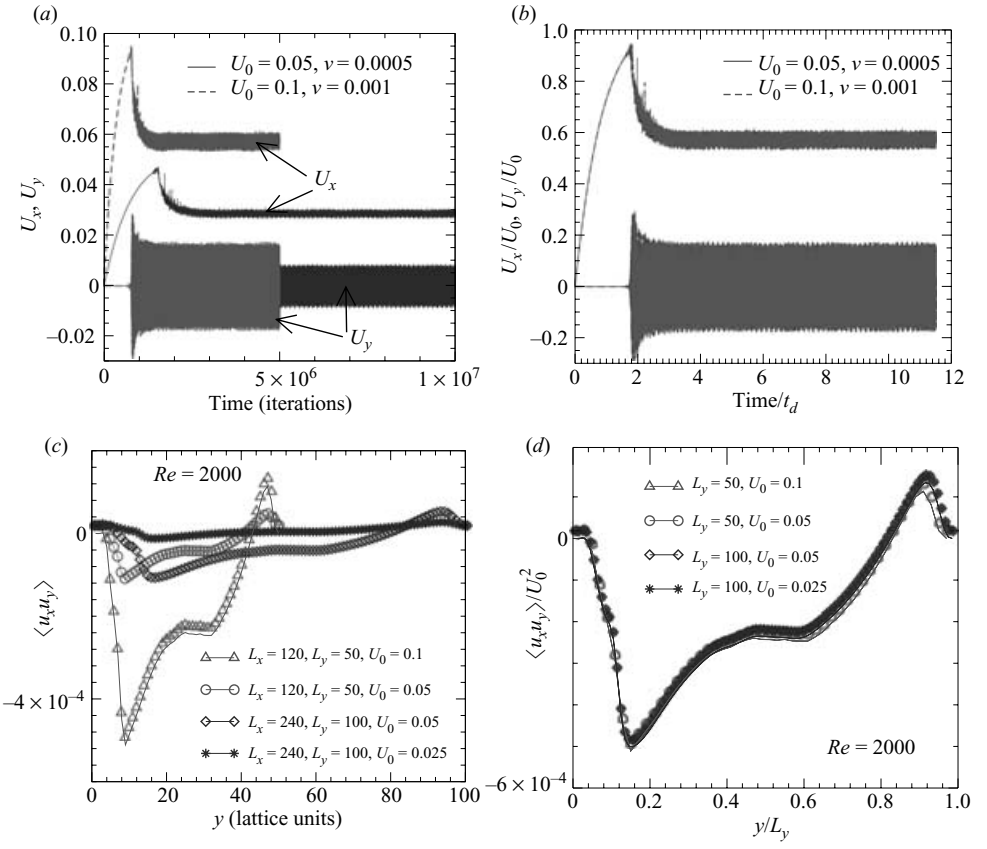

FIGURE 7. (a) U_x, and U_y versus time for two choices of the characteristic velocity, U_0. (b) The rescaled version of the data shown in (a). (c) The Reynolds stress for four different combinations of the channel size and U_0 as indicated. (d) The rescaled version of quantities in (c).

same in all four cases. Note also that the details of the wall roughness are scaled appropriately: the 5:20 zig-zag surface used in the case of $L_x \times L_y = 120 \times 50$ is replaced by a 10:40 zig-zag wall for the double-size channel. As seen from figure 7(c), the rescaled versions of all four curves for the Reynolds stress follow the same master curve in accord with the scaling properties of the NS-equation.

The test shown in figure 7(c, d) also provides useful information on the accuracy of the results with respect to the grid resolution. If the grid resolution were not satisfactory in order to capture the basic physics of the problem, a significantly different behaviour could be observed when comparing results for different system sizes (since a smaller system size would lead to a significantly larger error). Indeed, a close inspection of figure 7(d) reveals some small deviations when changing the system size, whereas, for a given system size, the rescaled Reynolds stresses obtained for different characteristic velocities are identical. These deviations are, however, quite small compared to the overall variation of the Reynolds stress. This observation strongly suggests that, even in the case of the smallest system studied ($L_x \times L_y = 120 \times 50$), our simulation results are accurate enough to describe the essential features of the phenomenon studied.

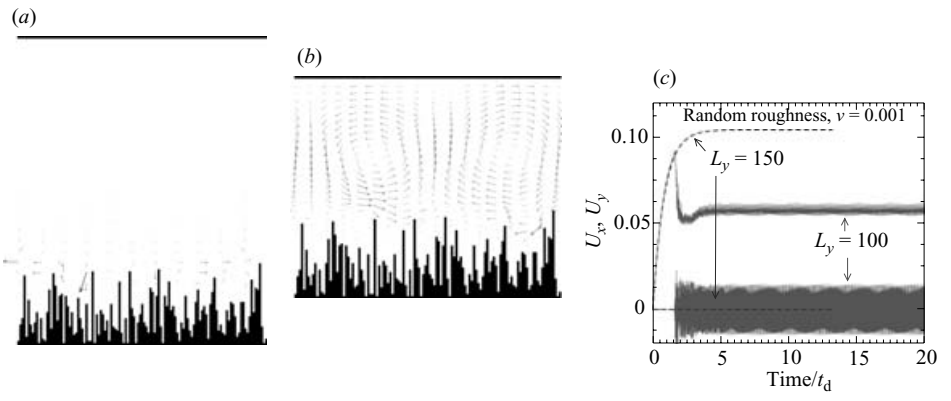

FIGURE 8. Impact of the channel width on flow instability. Velocity fluctuations are shown for two channels of widths $L_y = 150$ (*a*) and $L_y = 100$ (*b*). (*c*) The time evolution of the mid-channel velocities U_x and U_y for both cases.

Next we discuss the relevance of the observed roughness-induced transition to flow instability for strongly confined channels. This is the subject of figure 8 where velocity fluctuations are shown for two channels differing in the channel width only. Note that, here, the velocity fluctuations are defined in a slightly different way than previously, namely via $\boldsymbol{u}(x, y, t) = \boldsymbol{U}(x, y, t) - \bar{\boldsymbol{U}}(y, t)$, where $\bar{\boldsymbol{U}}(y, t) = \sum_{x=1}^{L_x} \boldsymbol{U}(x, y, t)/L_x$ is the *spatial* average of U_y along a horizontal line at y. The dynamic viscosity is the same for the both channel widths ($\nu = 0.001$) and the external force was tuned such that, in the case of a laminar flow, a mid-channel velocity of $U_0 \approx 0.1$ would be established in the steady state (equation (3.2)).

A laminar flow is observed in the channel with a width of $L_y = 150$ and the prescribed mid-channel velocity is reached (figure 8*c*). The Reynolds number for the flow in this channel is thus easily estimated as $Re = L_y U/(2\nu) = 7500$. The laminar character of the flow is nicely reflected in the behaviour of velocity fluctuations: with the exception of the near-wall region, no velocity fluctuations are found in the channel (figure 8*a*).

As the channel width is decreased from $L_y = 150$ to $L_y = 100$, strong velocity fluctuations appear, forming eddy like structures (figure 8*b*). Again, the emergence of flow instability in the narrower channel is accompanied by a sudden decrease of the streaming velocity and in the onset of strong fluctuations of the vertical component of the velocity. Now we observe $U \approx 0.06$ which corresponds to a Reynolds number of $Re = \approx 3000$.

The above comparison underlines the enhanced impact of the surface topography in narrow channels. The narrower the channel, the stronger the roughness-induced flow instability. Note that, in the case of the data shown in figure 8, the bottom wall is not made of a regular array of triangles but of a random distribution of obstacles. Even though not unexpected, the observation of flow instability in figure 8(*b*) underlines the fact that the phenomenon of roughness-induced flow instability is not restricted to the regular roughness types studied (arrays of triangles) but can also occur in the case of more complex roughness geometries.

Finally, we investigate the role of the wall roughness in generating perturbations of the velocity field. For this purpose, we monitor the velocity fluctuations at the beginning of flow instability. Snapshots of the velocity fluctuations for different times

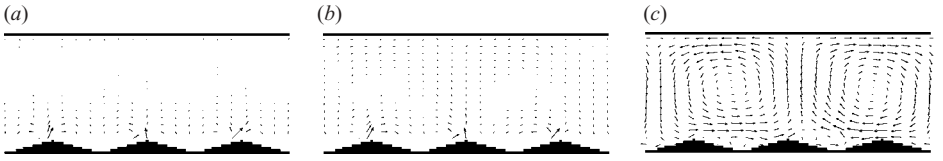

FIGURE 9. Snapshots of velocity fluctuations at the initial stages of flow instability in a channel of size 120×50 with a 5:20 zig-zag bottom wall ($\mathrm{Re} \approx 1600$). (*a*) $t = 8 \times 10^5$, (*b*) 8.5×10^5, (*c*) 9×10^5.

during the onset of flow instability are depicted in figure 9. Here, we study a channel of size $L_x \times L_y = 120 \times 50$ made up of a planar wall on the top and a 5:20 zig-zag wall on the bottom. The Reynolds number based on the mean mid-channel velocity is estimated to be $Re \approx 1600$.

The velocity fluctuations are defined as described in the context of figure 8. As seen from figure 9, velocity fluctuations are first generated in the vicinity of the rough wall, gradually giving rise to further fluctuations in the inner part of the channel. The rough wall, therefore, represents a stronger 'source' of fluctuations than the flat wall. This interpretation is also consistent with the results in figure 5, where profiles of fluctuating quantities are shown. Note also that the flow instability observed here is intimately related to the presence of the wall roughness: replacing the zig-zag wall by a flat one leads to a time-independent laminar flow.

We close this section by emphasizing that the phenomenon of roughness-induced transition to flow instability is not restricted to the extreme situations where the average height of roughness asperities is comparable to the channel width as outlined at the beginning of this section (figure 4*a*).

We have already discussed situations where the surfaces are much smoother. The data shown in figure 9 provide an example. Here, the channel width is a factor of two smaller than in the case shown in figure 4. Using the scaling property of the NS-equation, it then follows that, at a Reynolds number of $Re \approx 1600$, flow instability must also occur in the case of a channel of size 240×100 made up of a smooth wall on the top and a 10:40 zig-zag surface on the bottom. Note that a 10:40 zig-zag surface has one fourth the height but twice the roughness wavelength of the 40:20 zig-zag surface. Thus, a higher roughness wavelength allows the occurrence of flow instability at a much lower roughness height (Varnik & Raabe 2006).

5. Conclusions

Results of lattice Boltzmann simulations of roughness-induced flow instability are presented. The main observation is obtained by focusing on moderate Reynolds number flows in the case of strongly confined channels. Here, 'moderate' means that the Reynolds number is high in the sense that the advective term in the Navier–Stokes equation is not negligible compared to the viscous diffusion term but not high enough to give rise to flow instability/turbulence in channels made up of smooth walls. On the other hand, the term 'strongly confined' means that the average height of the surface asperities is of the same order as the channel width (figure 4).

As a first result, it is shown that it is possible to trigger a transition from a laminar to an unstable flow by an increase of the roughness height alone (figure 4). This holds for a variety of roughness types such as zig-zag walls with various aspect ratios and for walls with a random distribution of obstacles.

Various quantities relevant to unstable flows are investigated. Examples are standard deviations and the anisotropy of the velocity fluctuations (figure 5) as well as the spatial dependence of the viscous and Reynolds stresses (figure 6). The Reynolds stress is practically negligible in the case of viscous flows, whereas it becomes the dominant contribution to the total stress at sufficiently high surface roughnesses.

The physical significance of the results obtained is underlined by demonstrating that the sum of the viscous shear stress and the Reynolds stress obeys a linear law derived from the NS-equation. Furthermore, solutions obtained within the present simulations satisfy the transformation laws of the Navier–Stokes equation: when all quantities such as the fluid velocity and the Reynolds stress are expressed in appropriate units based on the characteristic velocity, length and time, the solution of the NS-equation is unique for all choices of the mean streaming velocity and the system size, provided that the Reynolds number and the channel shape are unchanged (figure 7).

A further observation concerns the impact of the wall roughness on the generation of the perturbations (figure 9). Monitoring the initial stages of the transition to flow instability, it is found that velocity fluctuations are first produced close to the rough wall before being propagated toward the inner part of the system. This is in line with the intuitive idea that a rough wall represents a stronger source of perturbations than a flat wall.

Similarly, a strong impact of the channel width on the transition to flow instability is observed. The wider the channel, the less pronounced the effects of a given wall roughness (figure 8) on the flow properties. This is intuitively appealing as it means that the relative impact of the surface roughness increases with decreasing channel width. At the same time, this observation underlines the importance of the surface roughness in micro-flows and in all cases where the roughness dimensions are comparable to the channel width.

Note that there are many practical situations where strongly confined flows at moderate and high Reynolds numbers may occur. An example of considerable industrial relevance is the flow of lubricant in a stamping experiment, where two plates are pushed towards one another reaching distances comparable to the height of surface asperities and pushing away the fluid between with high velocities.

Real flows occur in three-dimensional space, whereas we considered a two-dimensional problem only. However, since the flow instability considered here is intimately related to the presence of wall roughness (it disappears in the case of smooth walls) and to the confined geometry (it also disappears as the channel width is increased, see figure 8), the present phenomenon is different from that of the bulk turbulence where the vortex stretching term (absent in two-dimensional flows, see § 1) plays a major role. Roughness-induced flow instability may, therefore, also occur in three-dimensions, provided that the two major conditions are satisfied: confinement and relatively high surface corrugation.

Note, however, that other cases where the average roughness height is only a small fraction of the channel width are also discussed (figure 9) showing that the phenomenon is not restricted to the case of extremely confined channels and may occur in channels with less pronounced wall corrugation as well. In this respect, it is argued that the (average) roughness wavelength may play a crucial role in reducing the threshold Reynolds number for the occurrence of flow instability. This aspect is investigated in a recent paper (Varnik & Raabe 2006).

The phenomenon discussed in this paper may also find application in conjunction with recent developments of the lattice Boltzmann method to simulate heterogeneous boundary conditions (Succi 2002; Benzi *et al.* 2006). In Succi (2002), for example,

it is shown that wall roughness may increase the conversion efficiency of catalytic reactions in (micro-) channels considerably. Since the transition to flow instability allows a more efficient contact between the bulk fluid and the walls, one can expect that, for the Reynolds numbers and wall roughnesses considered in the present work, the impact of wall corrugation on the conversion efficiency may be further enhanced due to the onset of flow instability.

Despite the limitation of our studies to two-dimensional cases, we expect similar effects also in three dimensions. In fact, there are many more pathways for the advection of fluctuations in a higher dimensional space. Furthermore, the vortex stretching term present in three-dimensions leads to a more complex spatial and temporal variation of the vorticity, presumably enhancing the chaotic (unstable) character of the flow. The perturbations generated at the wall roughness are, therefore, expected to grow faster in the case of three-dimensional flows as the transition regime is approached. This suggests that, in three-dimensions, the phenomenon discussed here may be observable even at lower Reynolds numbers than in two-dimensions.

The possibility of triggering flow instability via adding/modification of wall roughness in real three-dimensional flows may open the way for a wide range of applications where flow instability/turbulence is desirable (e.g. turbulent mixing) but the Reynolds number cannot be increased arbitrarily. Tuning the wall roughness provides a new and independent way for controlling qualitative features of the flow. This aspect will be worked out in a future paper.

We acknowledge the financial support by the Deutsche Forschungsgemeinschaft (DFG) under the project numbers Do 794/1-1 and Va205/3-2 within the priority program SPP1164 "Nano-& Microfluidics".

REFERENCES

Ahlrichs, P. & Dünweg, B. 1999 Simulation of a single polymer chain in solution by combining lattice boltzmann with molecular dynamics. *J. Chem. Phys.* **111**, 8225.

Benzi, R., Biferale, L., Sbragaglia, M., Succi, S. & Toschi, F. 2006 Mesoscopic modelling of heterogeneous boundary conditions for microchannel flows. *J. Fluid Mech.* **548**, 257.

Benzi, R., Succi, S. & Vergassola, M. 1992 The lattice-Boltzmann equation – theory and applications. *Phys. Rep.* **222**, 145.

Chen, H., Kandasamy, S., Orszag, S., Shock, R., Succi, S. & Yakhot, V. 2003 Extended boltzmann kinetic equation for turbulent flows. *Science* **301**, 633.

Chen, S. & Doolen, G. D. 1998 Lattice Boltzmann method for fluid flows. *Annu. Rev. Fluid Mech.* **30**, 329.

Cornubert, R., d'Hummiières, D. & Levermore, D. 1991 A knudsen layer theory for lattice gases. *Physica* D **47**, 241.

Dupuis, A. & Chopard, B. 2003 Theory and applications of an alternative lattice boltzmann grid refinement algorithm. *Phys. Rev.* E **67**, 066707.

Filippova, O. & Hänel, D. 1998 Grid refinement for lattice bgk models. *J. Comput. Phys.* **147**, 219.

Filippova, O., Succi, S., Mazzocco, F., Arrighetti, C., Bella, G. & Hänel, D. 2001 Multiscale lattice boltzmann schemes with turbulent modeling. *J. Comput. Phys.* **170**, 812.

Frisch, U., Hasslacher, B. & Pomeau, Y. 1986 Lattice-gas automata for the Navier-Stokes equation. *Phys. Rev. Lett.* **56**, 1505–1508.

Frisch, U., d'Humiéres, D., Hasslacher, B., Lallemand, P., Pomeau, Y. & Rivet, J. P. 1987 Lattice gas hydrodynamics in two and three dimensions. *Complex Systems* **1**, 649–707.

Ginzbourg, I. & d'Humières, D. 1996 Local Second-order boundary methods for lattice Boltzmann models. *J. Stat. Phys.* **84**, 927.

Ginzbourg, I. & d'Humières, D. 2003 Multireflection boundary conditions for lattice boltzmann models. *Phys. Rev.* E **68**, 066614.

Gunstensen, A. K. & Rothman, D. H. 1993 Lattice-boltzmann studies of two-phase flow through porous media. *J. Geophys. Res.* **98**, 6431.

He, X. & Luo, L. S. 1997 Lattice Boltzmann model for the incompressible Navier-Stokes equation. *J. Stat. Phys.* **88**, 927.

Higuera, F., Succi, S. & Benzi, R. 1989 Lattice gas dynamics with enhanced collisions. *Europhys. Lett.* **9**, 345.

Krogstad, P.-A. & Antonia, R. A. 1999 Surface roughness effects in turbulent boundary layers. *Exps. Fluids* **27**, 450.

Ladd, A. J. C. & Verberg, R. 2001 Lattice-boltzmann simulations of particle-fluid suspensions. *J. Stat. Phys.* **104**, 1191.

Landau, L. D. & Lifschitz, E. M. 1991 *Hydrodynamik*, vol. VI. Berlin: Akademie Verlag.

Luo, L. S. 1997 Analytic solutions of linearized lattice boltzmann equations for simple flows. *J. Stat. Phys.* **88**, 913.

Mathieu, J. & Scott, J. 2000 *An Introduction to Turbulent Flow*. Cambridge University Press.

McNamara, G. & Zanetti, G. 1988 Use of boltzmann equation to simulate lattice-gas automata. *Phys. Rev. Lett.* **61**, 2332.

Mei, R., Yu, D., Shyy, W. & Luo, L.-S. 2002 Force evaluation in the lattice Boltzmann method involving curved geometry. NASA/CR-2002-211662, *ICASE Rep.* 2002-22.

Pope, S. B. 2000 *Turbulent Flows*. Cambridge University Press.

Prandtl, L. 1925 Bericht über die entstehung der turbulenz. *Z. Angew. Math. Mech.* **5**, 136.

Qian, Y. H., d'Humieres, D. & Lallemand, P. 1992 Lattice bgk models for Navier-Stokes equation. *Europhys. Lett.* **17**, 479.

Raabe, D. 2004 Overview of the lattice boltzmann method for nano- and microscale fluid dynamics in materials science and engineering. *Modelling Simul. Mater. Sci. Engng* **12**, R13.

Raupach, M. R., Antonia, R. A. & Rajagopalan, S. 1991 Rough-wall turbulent boundary layers. *Appl. Mech. Rev.* **44**, 1.

Rothman, D. H. & Zaleski, S. 1997 *Lattice-Gas Cellular Automata* (*Simple Models of Complex Hydrodynamics*). Cambridge University Press.

Rotta, J. C. 1962 Turbulent boundary layers in incompressible flow. In *Progress in Aeronautical Sciences* (ed. A. Ferri, D. Kuchemann & L. H. G. Sterne), vol. 2, p. 1. Pergamon.

Schlichting, H. 1979 *Boundary-Layer Theory*, 7th edn. McGraw-Hill.

Succi, S. 2001 *The Lattice Boltzmann Equation: for Fluid Dynamics and Beyond*. Series Numerical Mathematics and Scientific Computation. Oxford University Press.

Succi, S. 2002 Mesoscopic modeling of slip motion at fluid-solid interfaces with heterogeneous catalysis. *Phys. Rev. Lett.* **89**, 064502.

Succi, S., Filippova, O., Chen, H. & Orszag, S. 2002 Towards a renormalized lattice boltzmann equation for fluid turbulence. *J. Stat. Phys.* **107**, 261.

Varnik, F. & Raabe, D. 2006 Scaling effects in microscale fluid flows at rough solid surfaces. *Modelling Simul. Mater. Sci. Engng* **14**, 857.

Wolf-Gladrow, D. A. 2000 *Lattice-Gas Cellular Automata and Lattice Boltzmann Models*. Springer.

Xi, H., Peng, G. & Chou, S.-H. 1999 Finite-volume lattice boltzmann method. *Phys. Rev.* E **59**, 6202.